Contents lists available at ScienceDirect

Chemical Engineering Research and Design

journal homepage: www.elsevier.com/locate/cherd

Modeling for design and operation of high-pressure membrane contactors in natural gas sweetening

Ven Chian Quek[a,b], Nilay Shah[a], Benoît Chachuat[a,*]

[a] Centre for Process Systems Engineering, Department of Chemical Engineering, Imperial College London, South Kensington Campus, London SW7 2AZ, UK

[b] Group Research & Technology, PETRONAS, 50088 Kuala Lumpur, Malaysia

ARTICLE INFO

Article history:
Received 17 October 2017
Received in revised form 11 January 2018
Accepted 16 January 2018
Available online 31 January 2018

Keywords:
Membrane contactor
Natural gas sweetening
High-pressure operation
Membrane partial wetting
Experimental validation
Model-based analysis

ABSTRACT

Over the past decade, membrane contactors (MBC) for CO_2 absorption have been widely recognized for their large intensification potential compared to conventional absorption towers. MBC technology uses microporous hollow-fiber membranes to enable effective gas and liquid mass transfer, without the two phases dispersing into each other. The main contribution of this paper is the development and verification of a predictive mathematical model of high-pressure MBC for natural gas sweetening applications, based on which model-based parametric analysis and optimization can be conducted. The model builds upon insight from previous modeling studies by combining 1-d and 2-d mass-balance equations to predict the CO_2 absorption flux, whereby the degree of membrane wetting itself is calculated from the knowledge of the membrane pore-size distribution. The predictive capability of the model is tested for both lab-scale and pilot-scale MBC modules, showing a close agreement of the predictions with measured CO_2 absorption fluxes at various gas and liquid flowrates, subject to a temperature correction to account for the heat of reaction in the liquid phase. The results of a model-based analysis confirm the advantages of pressurized MBC operation in terms of CO_2 removal efficiency. Finally, a comparison between vertical and horizontal modes of operation shows that the CO_2 removal efficiency in the latter can be vastly superior as it is not subject to the liquid static head and remediation strategies are discussed.

© 2018 The Authors. Published by Elsevier B.V. on behalf of Institution of Chemical Engineers. This is an open access article under the CC BY license (http://creativecommons.org/licenses/by/4.0/).

1. Introduction

Natural gas (NG) is presently the third most-utilized form of fossil fuel energy and is widely used for both electricity production and transportation. In the reference case of the latest International Energy Outlook [IEA, 2017], the world's NG consumption is expected to increase by 69% between 2012 and 2040, accounting for 29% of the energy consuming market, and surpassing coal as the second most utilized fuel by 2030. NG consists of a mixture of combustible hydrocarbon gases typically from methane (CH_4) to pentane (C_5H_{12}), with impurities such as carbon dioxide (CO_2). Removal of CO_2 from NG is important for various reasons. The sales gas specification for NG typically imposes a CO_2 content lower than 2–3% [TransCanada, 2016]. In liquefied natural gas (LNG) plants, CO_2 should be removed further to meet the tight specification of <50 ppmv, so as to avoid freezing in low-temperature chillers (liquefaction process); and in ammonia plants likewise, CO_2 concentrations of <100 ppmv are needed to avoid catalyst poisoning [Boucif et al., 2012; Hoff, 2003]. As far as pipeline transport is concerned, CO_2 removal avoids pumping any extra volume of gas and reduces the risk of corrosion when moisture is present in process equipment and pipeline. Regarding NG utilization lastly, the presence of CO_2 reduces the heating value of NG.

Available CO_2 removal techniques based on physical and chemical principles include absorption, adsorption, cryogenic, carbonate looping, oxyfuel combustion, and membrane

* Corresponding author.
E-mail address: b.chachuat@imperial.ac.uk (B. Chachuat).
https://doi.org/10.1016/j.cherd.2018.01.033
0263-8762/© 2018 The Authors. Published by Elsevier B.V. on behalf of Institution of Chemical Engineers. This is an open access article under the CC BY license (http://creativecommons.org/licenses/by/4.0/).

separation. Chemical solvent absorption remains the most widely adopted technology to capture CO_2, using conventional packed, spray or bubble column absorption towers. About 90% of the acid gas treating processes in operation use alkanoamines solvents, such as methylethanolamine (MEA), diethanolamine (DEA), and methyldiethanolamine (MDEA), due to their versatility and ability to remove acid gases to ppm levels [Paul et al., 2007]. Nonetheless, conventional absorption towers have a high capital cost and a large physical footprint, and they are subject to operational problems such as flooding, channeling, foaming and liquid entrainment [Gabelman and Hwang, 1999]. Membrane technology has been applied since the 1980s for CO_2 removal in large-scale applications due to their potential to reduce the footprint and the capital and operating costs [He and Hägg, 2012]. However, the usual gas separation membranes have a relatively low permeability, and their low selectivity can lead to large product loss.

By combining membranes and solvents, membrane contactors (MBC) offer a unique way to perform gas–liquid absorption [Gabelman and Hwang, 1999]. The microporous membrane acts as a non-selective phase barrier, allowing the liquid and gas phases to contact with each other, yet without the dispersion of one phase into the other. This barrier prevents flooding or foaming issues from happening, thereby making MBC simple to operate. Their packaging into hollow-fiber membrane (HFM) modules offers a higher mass transfer area compared with conventional packed columns, giving MBC a high intensification potential [Rangwala, 1996; Favre, 2011]. This modularity also empowers a more flexible design and scale-up. The effectiveness of MBC for both pre- and post-combustion CO_2 capture, as well as NG sweetening and dehydration, has been extensively studied and compared with conventional techniques over the past decades; see, e.g., review papers by [Mansourizadeh and Ismail, 2009; Favre, 2011; He and Hägg, 2012; Hoff and Svendsen, 2014]. In NG sweetening for instance, Hoff and Svendsen (2013) reported a 75% size reduction using MBC compared to conventional packed columns. This technology has been embraced by industry too, with recent patents on acid gas removal from NG granted to Petroliam Nasional Berhad (PETRONAS) [Quek et al., 2015] and the Gas Technology Institute (GTI) [Zhou and Meyer, 2014].

Notwithstanding their high potential, MBC can present rather low mass-transfer coefficients under undisturbed, laminar flow of the liquid phase. Moreover, hydrophobic membranes can be wetted by organic solvents, either partially or fully. The non-wetted mode of MBC operation (Fig. 1a) is preferred since it presents a higher CO_2 absorption rate. Operating with partially- or fully-wetted membranes (Fig. 1b, c) can decrease the mass-transfer flux quite drastically, mainly due to a lower gas diffusivity in the wetted membrane phase. For instance, Wang et al. (2005) reported that a change in the degree of wetting as small as 5% could lead to a 20% reduction in mass transfer rate. In principle, membrane wetting could be prevented by keeping the operating pressure below a critical value, the so-called breakthrough pressure; but partial-wetting may still occur in practice due to non-uniform membrane pore-sizes, with bigger pores being more easily wetted. Many factors are known to affect the degree of wetting, including the membrane properties and various operating parameters, such as the inlet liquid pressure, liquid velocity, liquid temperature, and amine concentrations [Lu et al., 2008; Mosadegh-Sedghi et al., 2012; Rongwong et al., 2015]. Moreover, the variation in liquid pressure along the length of the HFM can affect membrane wetting considerably, e.g. due to pressure drops or the static head in a vertical MBC.

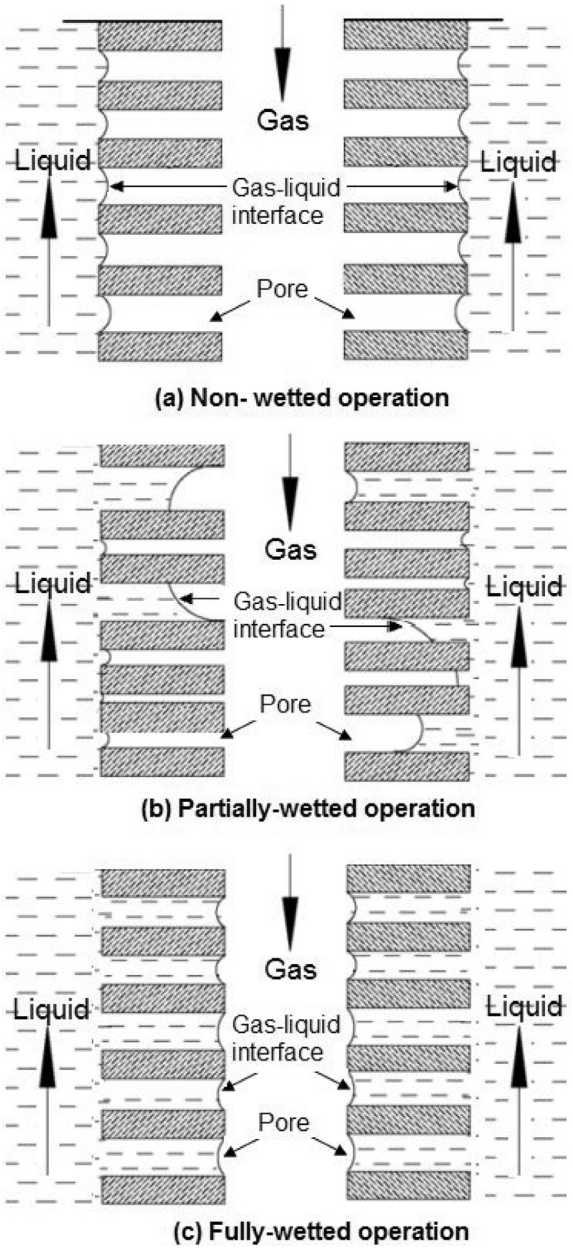


Fig. 1 – Different degrees of membrane wetting in MBC operation.
Adapted from: Lu et al. (2008).

Mathematical models provide an effective tool to help understand the CO_2 removal mechanisms in MBC, and thus enable a better assessment and optimization of their performance. Many modeling and simulation studies in the literature focus on the non-wetted mode of operation, e.g. for MBC operating at or near atmospheric pressure [Hoff et al., 2004; Al-Marzouqi et al., 2008; Rezakazemi et al., 2011; Hoff and Svendsen, 2014]. When partially- or fully-wetted operation is considered, the degree of membrane wetting (or a related parameter) is typically used as a tuning parameter in order for the model predictions to fit given experimental data. For instance, Chabanon et al. (2013) compared several modeling approaches for predicting CO_2 absorption in MBC, ranging from constant mass-transfer coefficient models to 1-d or 2-d convection-diffusion models, and with the membrane mass-transfer coefficient used as the single tuning parameter. They

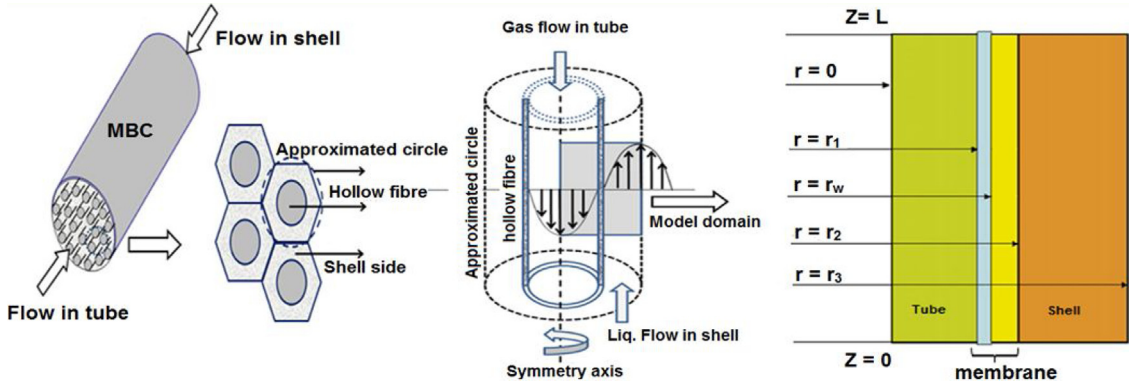


Fig. 2 – Modeling framework for a counter-current, follow fiber MBC module. Left: cylindrical approximation around each fiber. Center: single piece of hollow fiber. Right: spatial domains in MBC model.

found that the use of convection-diffusion models is justified to obtain accurate predictions, in particular when large amine solvent conversions take place. Other studies showing a good agreement between experimental data and the predictions of a 2-d convection-diffusion model by adjusting the degree of membrane wetting can be found in Lu et al. (2008) and Cui et al. (2015). As far as high-pressure MBC operation is concerned, e.g. for NG sweetening applications, limited modeling studies have been published to date. For instance, Faiz and Al-Marzouqi (2010) studied the removal of CO_2 from NG in high-pressure MBC between 10 and 50 bar. They reported a good agreement between a 2-d model and experiments when adjusting the degree of wetting, which also they found to be highly sensitive.

Because of this high sensitivity of the membrane wetting to different operating conditions, analyzing or optimizing the performance of an MBC under the assumption of a constant membrane wetting could lead to erroneous (over-optimistic) results. In response to this, approaches to predicting the degree of membrane wetting in MBC have started to appear in recent years. The studies by Boributh et al. (2011) and Goyal et al. (2015) in particular, exploit knowledge about a membrane's pore-size distribution to predict the degree of wetting in MBC operating at atmospheric pressure.

The main objective of this paper is the development of a predictive mathematical model of high-pressure MBC for NG sweetening applications, on the basis of which model-based parametric studies and optimization can be conducted. Building upon previous modeling studies, we consider a combination of 1-d and 2-d mass-balance equations to predict the CO_2 absorption flux, whereby the degree of membrane wetting itself is calculated using the Laplace–Young equation based upon knowledge of the membrane pore-size distribution, and real gas behavior too is accounted for at high-pressure operation. The predictive capability of this model is tested against data from two experimental settings: a lab-scale MBC module, where the purification is conducted using binary gas mixtures of CH_4/CO_2 and N_2/CO_2 at 11 bar; and a pilot-scale MBC module operated under industrially relevant conditions at a natural gas processing plant in Malaysia. All of the experiments were conducted with aqueous mixtures of MDEA and piperazine (PZ) as the chemical solvent. This ability to predict the variation in membrane wetting along the fiber length makes it possible to analyze the effects of various design and operational decisions on the MBC performance, including the membrane properties, module characteristics, gas and liquid flow rates, and operating pressures and temperatures.

The rest of the paper is organized as follows. The mathematical model of a counter-current hollow-fiber MBC module is presented in Section 2, followed by a description of both experimental set-ups, corresponding model parameters, and computational methods in Section 3. Results of the experimental model verification are presented and discussed in Section 4. Then, a model-based analysis is conducted in Section 5, with a view to quantifying the effects of module orientation and high-pressure operation on a module's CO_2 removal efficiency. Finally, Section 6 concludes the paper and discusses future research directions.

2. Modeling of high-pressure hollow-fiber MBC

This section of the paper describes a comprehensive mathematical model for predicting the CO_2 removal efficiency in a high-pressure, hollow-fiber MBC module, as depicted on the left panel in Fig. 2. The NG gas mixture containing CO_2 flows through the membrane fibers, while the amine solvent flows inside the shell, in a counter-current arrangement. The gas mixture diffuses from the tube side through the fiber walls into the shell, where CO_2 dissolves in the solvent before reacting with the solvent in order to enhance the removal rate.

The shell area between the fibers depends on the packing density, $\emptyset$ defined as

$$\emptyset = N\frac{r_2^2}{R_m^2}, \tag{1}$$

where N is the number of fibers in the MBC module; R_m [m] is the inner radius of the module; and r_2 [m] is the outer radius of the fibers. Following Happel (1959), the domain of fluid surrounding each fiber can be conveniently approximated by a cylinder with cross-section radius, r_3 [m] given by

$$r_3 = r_2\sqrt{1/\emptyset}. \tag{2}$$

It is thus sufficient to consider a piece of hollow fiber in order to model the MBC module, as shown on the center panel in Fig. 2.

In order to describe the degree of membrane wetting, we introduce the so-called wetted radius, r_w [m], a conceptual variable representing the average fraction of membrane pores filled with liquid; see Section 2.1 below for details. The non-wetted and fully-wetted modes of operation thus correspond to $r_w = r_1$ and $r_w = r_2$, respectively, with r_1 the inner radius of the fibers. On exploiting symmetry, the spatial domain

to model a piece of hollow fiber can be taken as $(r, z) \in [0, r_3] \times [0, L]$, which is further partitioned into four subdomains as shown on the right panel in Fig. 2: (i) tube, $0 \le r \le r_1$; (ii) membrane-dry, $r_1 \le r \le r_w(z)$; (iii) membrane-wet, $r_w(z) \le r \le r_2$; and (iv) shell, $r_2 \le r \le r_3$. Notice that the geometry of the wetted and non-wetted membrane subdomains is complicated by the dependence of the wetted radius on the axial position, z. In this counter-current configuration, the solvent and the gas are fed at z = 0 and z = L, respectively. Mass conservation equations and a corresponding set of boundary conditions are detailed in Section 2.2.

2.1. Modeling of membrane wetting

In partially-wetted operations, a hydrophobic membrane with a non-uniform pore size distribution exhibits a range of breakthrough pressures, with larger pores filled first, followed by smaller ones. According to the Laplace–Young equation, a pore is wetted when the transmembrane pressure difference ΔP_{TMPD} [Pa], is greater than the breakthrough pressure, ΔP_c [Pa] given by

$$\Delta P_c(\delta) = \frac{-2\gamma \cos\theta}{\delta}, \tag{3}$$

where δ [m] denotes the pore radius; γ [N m^{-1}], the surface tension of the liquid phase; and θ [rad], the contact angle of the liquid on the membrane.

The transmembrane pressure, namely the difference between the pressures in the liquid and gas phases, P_l and P_g [Pa], is such that

$$\Delta P_{TMPD}(z) = P_l(z) - P_g(z) = \begin{cases} P_l^{out} - \dfrac{P_l}{\Delta z}(L - z) - P_g^{in} & \text{horizontal orientation} \\ P_l^{out} - \dfrac{\Delta P_l}{\Delta z}(L - z) + \rho_l g(L - z) - P_g^{in} & \text{vertical orientation} \end{cases} \tag{4}$$

where P_g^{in} [Pa] is the inlet gas pressure; P_l^{out} [Pa], the outlet liquid pressure; $\Delta P_l/\Delta z$ [Pa m^{-1}], the pressure gradient along the shell axis; ρ_l [kg m^{-3}], the liquid density; and $g = 9.81$ m s^{-2} is the gravitational acceleration. Notice the additional contribution of the liquid static head in a vertical orientation compared with a horizontal MBC. Moreover, the pressure of the gas phase is considered constant in Eq. (4), i.e. the effects of the pressure drop and static head are neglected. One way of expressing the pressure drop in the shell is by using an analogy with viscous flow through assemblages of cylinders. Under the assumption of a constant pressure drop in the flow direction and a no-slip condition on the cylinders, Happel (1959) showed that the pressure drop may be computed as

$$\frac{\Delta P_l}{\Delta z} = -8\mu_l \overline{v_l} \frac{r_3^2 - r_2^2}{4r_2^2 r_3^2 - r_2^4 - 3r_3^4 - 4r_3^4 \ln(r_2/r_3)}, \tag{5}$$

where μ_l [kg m^{-1} s^{-1}] is the dynamic viscosity of the liquid phases; and the average liquid velocity, $\overline{v_l}$ [m s^{-1}] is given by

$$\overline{v_l} = \frac{F_l^{in}}{\pi R_m^2 (1 - \emptyset)}, \tag{6}$$

with F_l^{in} [m^3 s^{-1}] the liquid volumetric flowrate at the shell inlet z = 0.

In order to prevent membrane wetting and bubble formation, an MBC should ideally be operated such that

$$\Delta P_c(\delta) \ge \Delta P_{TMPD}(z) \ge 0, \tag{7}$$

for all pore radii and all axis positions. If partial wetting occurs at a given position $0 \le z \le L$, the wet pores are those having a radius larger than δ_w [m], given by

$$\delta_w(z) = \frac{-2\gamma \cos\theta}{\Delta P_{TMPD}(z)}. \tag{8}$$

In practice, the degree of wetting is often described in term so of the wetting ratio, $\mathfrak{Z}$, which represents the ratio between the porous-volume occupied by liquid phase and the total porous-volume. Under the assumption that the wetted pores are completed filled with liquid (see Goyal et al. (2015) for a discussion), the wetting ratio may be computed as

$$\mathfrak{Z}(z) = \frac{\int_{\delta_w(z)}^{\delta_{max}} \delta^2 f(\delta)\, d\delta}{\int_0^{\delta_{max}} \delta^2 f(\delta)\, d\delta}, \tag{9}$$

for a given pore size distribution (PSD) function f, and a maximal pore radius, δ_{max} [m]. Then, the conceptual wetted radius r_w representing the average fraction of a pore filed with liquid at a certain position z (see right panel in Fig. 2) is related to the wetting ratio $\mathfrak{Z}$ in the following way

$$r_w(z) = r_2 - [r_2 - r_1]\mathfrak{Z}(z). \tag{10}$$

2.2. Mass conservation equations

The mathematical model presented hereafter is based on steady-state and isothermal operation in all of the phases—see Section 4 for further discussions about the effect of temperature. The mass conservation equations in the gas, liquid and membrane phases are detailed in the following paragraphs, together with the corresponding boundary conditions and the main modeling assumptions.

2.2.1. Gas phase in tube, $(r, z) \in [0, r_1] \times [0, L]$

We describe the gas phase in the lumen using a simple plug flow, assuming homogeneous concentrations in each cross-section and neglecting the gas diffusivity (Péclet > 10^6) and pressure drops along the fiber axis. These assumptions have been validated through previous studies in MBC modeling [Rezakazemi et al., 2011; Goyal et al., 2015]. Moreover, due to operation at elevated pressures, we account for real gas behavior using a compressibility factor correction, calculated with the Peng–Robinson (PR) equation of state.

Mass conservation in the tube expresses the fact that the reduction in flux along the fiber axis is equal to the flux passing through the membrane. The differential equations describing the average velocity of the gas phase, $\overline{v_g}$ [m s^{-1}] and the average CO_2 concentration, $\overline{C_{CO_2}}$ [mol m^{-3}] are

$$\frac{d\overline{v_g}(z)}{\partial z} = -\frac{2D_{CO_2,md}}{r_1}\frac{ZRT_g}{P_g^{in}}\frac{\partial C_{CO_2}(r,z)}{\partial r}\Big|_{r=r_1^+}, \tag{11}$$

$$\frac{d\overline{C_{CO_2}}(z)}{\partial z} = -\frac{2D_{CO_2,md}}{\overline{v_g}(z)\,r_1}\left[1-\frac{ZRT_g\overline{C_{CO_2}}(z)}{P_g^{in}}\right]\frac{\partial C_{CO_2}(r,z)}{\partial r}\Big|_{r=r_1^+}, \tag{12}$$

where r_1^+ indicates the gas-membrane interface at the pore side; T_g [K] is the temperature of the gas; Z [–], the compressibility factor; $R = 8.3145\ m^3\,Pa\,mol^{-1}\,K^{-1}$, the gas constant; and $D_{CO_2,md}$ $\left[m\ s^{-2}\right]$ denotes the effective CO_2 diffusion coefficient in the dry part of the membrane, such that

$$D_{CO_2,md} = \frac{\varepsilon}{\tau}D_{CO_2,g}, \tag{13}$$

with $D_{CO_2,g}$ $[m\ s^{-2}]$, the diffusion coefficient of CO_2 in the gas phase; and ε, τ, the porosity and tortuosity of the membrane, respectively. Initial conditions at the inlet $z = L$ of the fiber are given by

$$\overline{v_g}(L) = \overline{v}_g^{in} = \frac{M_g^{in}}{N\pi r_1^2\rho_g}, \tag{14}$$

$$\overline{C_{CO_2}}(L) = C_{CO_2}^{in} = \frac{y_{CO_2,g}^{in}P_g^{in}}{ZRT_g}, \tag{15}$$

where M_g^{in} $[kg\ s^{-1}]$ is the inlet mass flowrate of gas; $y_{CO_2,g}^{in}$ [–], the inlet molar fraction of CO_2; and ρ_g $[kg\,m^{-3}]$, the density of the gas phase is the density of gas.

2.2.2. *Liquid phase in shell, (r, z) ∈ [r2, r3] × [0, L]*

The liquid flow in the shell is laminar (Reynolds <10), and we assume here that the velocity profile is fully developed, following Happel's free surface model [Happel, 1959]. Moreover, we neglect axial diffusivity in the liquid phase (Péclet $>10^7$), and we assume that the liquid phase is incompressible and that the reaction between CO_2 and the solvent does not incur any change in volume.

The general transport equation for a species $i \in \{CO_2, sol\}$ at steady state in the 2-d cylindrical coordinate system (r, z), taking into account convection, radial diffusion and reaction, reads [Cussler, 2009]:

$$v_l(r)\frac{\partial C_i(r,z)}{\partial z} = D_{i,l}\left[\frac{\partial C_i(r,z)}{\partial r^2}+\frac{1}{r}\frac{\partial C_i(r,z)}{\partial r}+\frac{\partial^2 C_i(r,z)}{\partial z^2}\right] + R_i(C_i(r,z)), \tag{16}$$

where $D_{i,l}$ $[m\,s^{-2}]$ and R_i $[mol\,m^{-3}\,s^{-1}]$ denote the diffusion coefficient and the reaction rate of the species i in the liquid phase, respectively; and v_l $[m\ s^{-1}]$ is the local fluid velocity, which by analogy with viscous flow through assemblages of cylinders—compare Eq. (5)—may be computed as [Happel, 1959]

$$v_l(r) = -\frac{1}{4\mu_l}\left[r^2 - r_2^2 + 2r_3^2 ln\left(\frac{r_2}{r}\right)\right]\frac{\Delta P_l}{\Delta z} = 2\overline{v_l}\left(r_3^2-r_2^2\right)\frac{r^2-r_2^2+2r_3^2\ln(r_2/r)}{4r_2^2r_3^2-r_2^4-3r_3^4-4r_3^4\ln(r_2/r_3)}. \tag{17}$$

The distribution of the CO_2 and solvent at the shell inlet are supposed to be uniform,

$$C_{CO_2}(r,0) = f_{CO_2,l}^{in}C_{sol}^{in}, \tag{18}$$

$$C_{sol}(r,0) = C_{sol}^{in}, \tag{19}$$

with C_{sol}^{in} $[mol\ m^{-3}]$ the solvent concentration in the liquid feed; and $f_{CO_2,l}^{in}$ $[mol\ mol^{-1}]$, the CO_2 loading in solvent. At the shell outlet, a no-dispersion condition is defined as

$$\frac{\partial C_i(r,z)}{\partial z}\Big|_{z=L} = 0, \quad i \in \{CO_2, sol\}. \tag{20}$$

Moreover, the condition of axisymmetric flow condition at $r = r_3$ gives

$$\frac{\partial C_i(r,z)}{\partial z}\Big|_{r=r_3} = 0, \quad i \in \{CO_2, sol\}, \tag{21}$$

while continuity of the concentrations and fluxes at the membrane surface, $r = r_2$ impose

$$C_i\left(r_2^+, z\right) = C_i(r_2^-, z), \quad i \in \{CO_2, sol\}, \tag{22}$$

$$D_{i,l}\frac{\partial C_i(r,z)}{\partial z}\Big|_{r=r_2^+} = D_{i,mw}\frac{\partial C_i(r,z)}{\partial z}\Big|_{r=r_2^-}, \quad i \in \left\{CO_2, sol\right\}, \tag{23}$$

where the radial positions r_2^+ and r_2^- correspond to either sides of the liquid-membrane interface; and $D_{i,mw}$ $[m\,s^{-2}]$ denotes the effective diffusion coefficient of a species i in the wetted part of the membrane, such that

$$D_{i,mw} = \frac{\varepsilon}{\tau}D_{i,l}. \tag{24}$$

2.2.3. *Membrane phase, (r, z) ∈ [r1, r2] × [0, L]*

The membrane properties are considered to be uniform along the fiber axis, including pore size distribution, tortuosity, porosity, thickness, and hydrophobicity. We assume that mass transfer inside the membrane is driven by radial diffusion only, considering the gas and liquid phases to be stagnant therein, and that Henry's law is applicable at the gas–liquid interface. Furthermore, we neglect the dissolution of gas species other than CO_2 into the liquid phase, and we consider the amine solvent to be non-volatile.

The partial differential equations describing the transport of CO_2 and solvent inside the membrane are given by

$$D_{CO_2,md}\left[\frac{\partial C_{CO_2}(r,z)}{\partial r^2}+\frac{1}{r}\frac{\partial C_{CO_2}(r,z)}{\partial r}\right] = 0 \quad \text{if} \quad r_1^+ \le r \le r_w^-(z), \tag{25}$$

$$D_{i,mw}\left[\frac{\partial C_i(r,z)}{\partial r^2}+\frac{1}{r}\frac{\partial C_i(r,z)}{\partial r}\right] + R_i\left(C_i(r,z)\right) = 0, \quad i \in \left\{CO_2, sol\right\} \quad \text{if} \quad r_w^+(z) \le r \le r_2^-. \tag{26}$$

The equilibrium condition at the gas–liquid interface, $r = r_w(z)$ inside the membrane is expressed as

$$C_{CO_2}\left(r_w^-(z), z\right) = \frac{H_{CO_2}}{ZRT_g}C_{CO_2}\left(r_w^+(z), z\right), \tag{27}$$

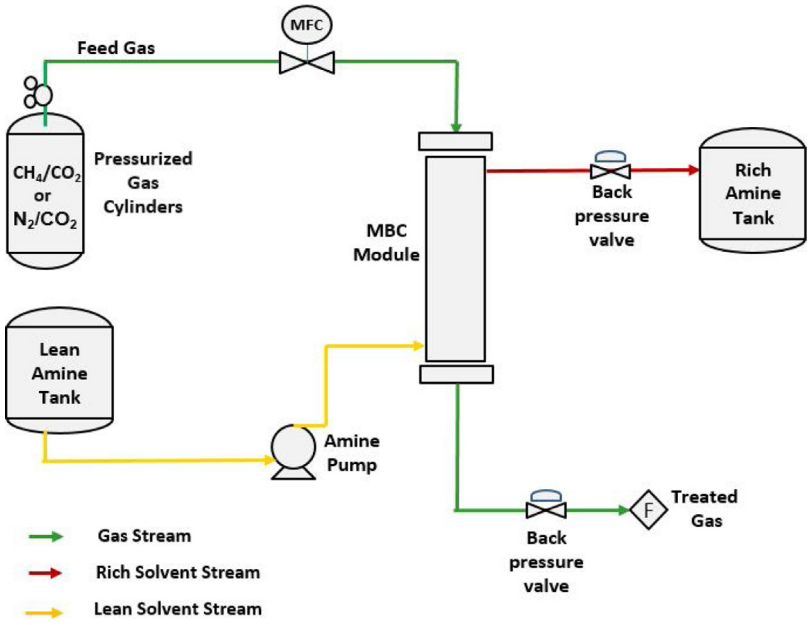


Fig. 3 – Schematic of the lab-scale setup for CO_2 removal using high pressure MBC.

where r_w^+ and r_w^- indicate either sides of the gas–liquid interface inside the membrane; H_{CO_2} [m^3 Pa mol^{-1}] stands for Henry's constant for CO_2 in amine solution; and T_l [K] is the temperature of the liquid phase. At this interface, the flux of solvent is equal to zero, while the flux of CO_2 is continuous,

$$D_{CO_2,md}\left.\frac{\partial C_{CO_2}(r,z)}{\partial z}\right|_{r=r_w^-(z)} = D_{CO_2,mw}\left.\frac{\partial C_{CO_2}(r,z)}{\partial z}\right|_{r=r_w^+(z)}, \quad (28)$$

$$\left.\frac{\partial C_{sol}(r,z)}{\partial z}\right|_{r=r_w^+(z)} = 0. \quad (29)$$

At the membrane–gas interface, $r = r_1$, the CO_2 concentration is continuous,

$$C_{CO_2}\left(r_1^+, z\right) = \overline{C_{CO_2}}(z), \quad (30)$$

and the CO_2 flux continuity is already expressed in Eq. (12). The concentration and flux continuity conditions at the membrane–liquid interface, $r = r_2$ are given in Eqs. (22) and (23) above.

3. Material and methods

3.1. *Experimental setups*

The lab-scale module experiments were conducted with the binary feed gas mixtures of CH_4/CO_2 and N_2/CO_2 at 11 bar, while the pilot module was up-scaled by a factor of about 800 (i.e. membrane area) to be operated under industrially relevant operating conditions at 54 bar in a natural gas processing plant in Malaysia. In both cases, aqueous mixtures of methyldiethanolamine (MDEA) and piperazine (PZ) were used as the chemical solvent. The corresponding operating conditions are summarized in Table 1. The experimental set-ups for lab- and pilot-scale testing are depicted in Figs. 3 and 4, with further details given thereafter.

3.1.1. *Lab-scale MBC module*

Pressurized gas cylinders were used to supply mixtures of CH_4/CO_2 or N_2/CO_2 to the tube side of the lab-scale module, while the lean amine solvent was pumped through the shell side, in a counter-current and vertical configuration. The feed gas and solvent flow rates were controlled using a mass flow controller (MFC) and pump stroke, respectively. The compositions of the feed gas and treated gas were analyzed and recorded using gas chromatography (GC7900, Shanghai Techcomp Instruments Co., Ltd), after the system had reached steady state as indicated by a constant CO_2 composition in the outlet gas stream of the module. The treated gas from the MBC module was then depressurized and vented to a safe location. A transmembrane pressure of ΔP_{TMPD} = 30 kPa was maintained at any point along the fibers in order to prevent gas bubbling [Kang et al., 2017].

3.1.2. *Pilot-scale MBC module*

The CO_2-rich natural gas was fed to the tube side of the MBC, while the lean amine was pressurized to ca. 54 bar and fed to the shell side, in a counter-current and vertical configuration. The feed gas and liquid flow rates were controlled using a mass flow controller and a pump stroke, respectively. The flowrate of the treated gas at the MBC outlet was measured with a mass flowmeter before sending it to the flare header. The enriched amine solvent collected from the MBC shell outlet was directed to a flash drum for degassing of any volatile and dissolved light hydrocarbons. The gas compositions in the MBC feed and outlet as well as the flash outlet were analyzed and recorded using gas chromatography (PGC1000 Gas Chromatograph, ABB) after the system had reached steady state. The flash liquid outlet stream was heated by cross exchange with hot lean solvent, and then fed to the solvent regenerator where it was stripped of acid gas by rising stream vapors generated by the reboiler. The acid gas leaving the top of the regenerator was cooled and sent to a reflux drum to separate the condensed water from the acid gas. The condensed water was then returned to the top of the regenerator, while the acid gas was sent to the flare header.

Table 1 – Operating conditions in the lab and pilot plant.

Parameters	N_2/CO_2 (lab)	CH_4/CO_2 (lab)	NG (pilot)
CO_2 inlet, $y^{in}_{CO_2,g}$ [mol%]	8	8.55	5.1–5.3
MDEA/PZ inlet [wt%]	39/5	39/5	39/5
Inlet gas pressure, P^{in}_g [kPa]	1100	1100	5400
Outlet liquid pressure, P^{out}_l [kPa]	1130	1130	5430
Gas mass flowrate, M^{in}_g [kg h^{-1}]	0.04–0.2	0.05–0.1	57–75
Liquid volumetric flowrate, F^{in}_l [L h^{-1}]	0.6–1.8	1.2	190–280
Gas temperature, T_g [K]	293	293	298–313
Liquid temperature, T_l [K]	293	308	308–313
CO_2 loading in solvent, $f^{in}_{CO_2,l}$ [mol mol^{-1}]	0	0.07	0.01

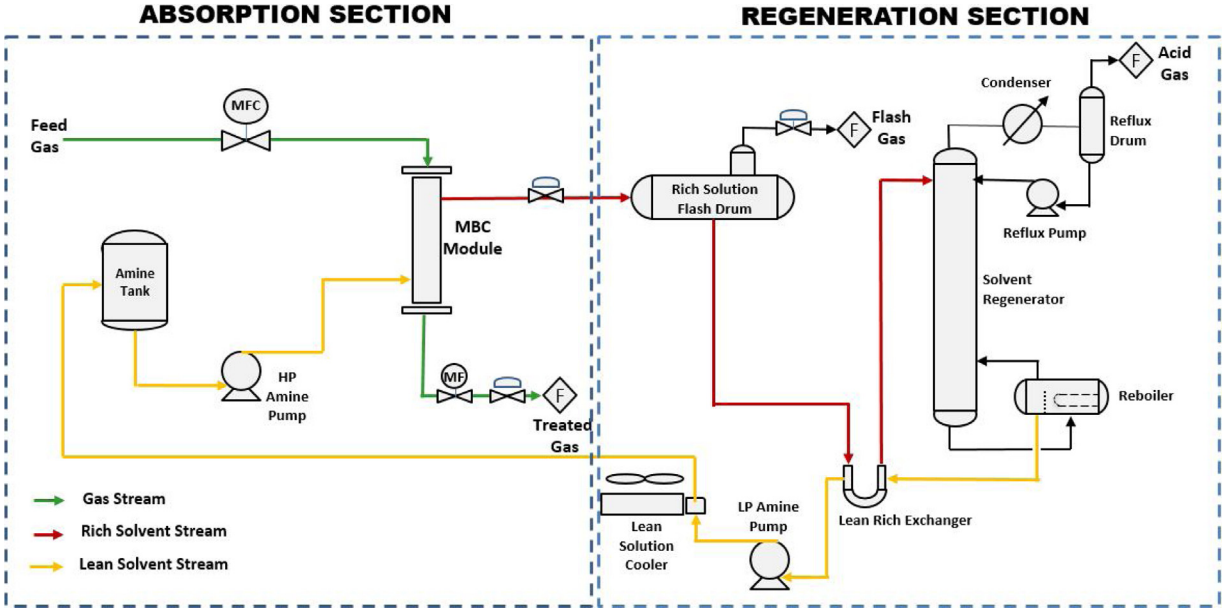


Fig. 4 – Schematic of the pilot-plant setup for CO_2 removal using high pressure MBC.

3.2. *Membrane and module characteristics*

The high pressure MBC modules were packed with hydrophobic, polytetrafluoroethylene (PTFE) hollow fiber. Table 2 reports the main characteristics of these membranes, alongside geometrical properties of the MBC modules used for lab- and pilot-scale testing.

Following Iversen et al. (1997), a first approximation of the membrane tortuosity in Table 2 was obtained as

$$\tau = \frac{(2-\varepsilon)^2}{\varepsilon}. \tag{31}$$

In order to determine the wetting ratio in Eq. (9) needed for simulating the MBC model, pore-size distribution (PSD) data from the manufacturer were used to fit the following log-normal distribution [Zydney et al., 1994; Lu et al., 2008]

$$f(\delta) = \frac{1}{\sqrt{2\pi\,\ln(1+\sigma^2)}\bar{\delta}} \exp\left(-\frac{(\ln \delta/\bar{\delta})^2(1+\sigma^2)}{2\,\ln(1+\sigma^2)}\right), \tag{32}$$

where $\bar{\delta}$ and σ stand for the mean pore radius and standard deviation, respectively. The resulting least-squares fit on the left plot in Fig. 5 shows an excellent agreement with the data, and the estimated values for $\bar{\delta}$ and σ can be found in Table 2. In turn, a surrogate relationship for the wetting ratio $\mathfrak{Z}$ as a function of the critical pore radius δ_w in the range $[0, \delta_{max}]$ could be obtained in the form

$$\mathfrak{Z}(\delta_w) = \frac{1+\tanh(a_0 + a_1(\delta_w/\bar{\delta}) + a_2(\delta_w/\bar{\delta})^2 + a_3(\delta_w/\bar{\delta})^3)}{2}, \tag{33}$$

with $a_0 = 7.966$, $a_1 = -14.08$, $a_2 = 8.418$, and $a_3 = -2.041$. A comparison between the solution of Eq. (9) and the surrogate in Eq. (33) is shown on the right plot in Fig. 5.

3.3. *Thermo-physical, transport, and reaction kinetic data*

Temperature-dependent expressions for (i) the macroscopic reaction rates of CO_2 with MDEA and PZ, (ii) Henry's constants for CO_2 in the amine solution, and (iii) the diffusivity coefficients of the various species in gas or liquid mixtures are reported in Appendix A for completeness. Values for the other thermo-physical and transport parameters were obtained by interfacing gPROMS with the property packages 'Advanced Peng Robinson' and 'UNIQUAC-RK'.

3.4. *Numerical simulation*

The mixed set of algebraic, ordinary differential and partial differential equations was implemented in the gPROMS modeling language [Oh and Pantelides, 1996], using ModelBuilder v5.0. A second-order centered finite difference scheme was used to discretize the differential equations, after a rescaling

Table 2 – Specifications of the hollow-fiber membranes and the lab- and pilot-scale modules.

Parameters	Lab module	Pilot module	Source
Fiber length, L [m]	0.3	2	Manufacturer
Fiber inner radius, r_1 [μm]	431	431	Manufacturer
Fiber outer radius, r_2 [μm]	846	846	Manufacturer
Membrane porosity, ε [–]	0.41	0.41	Manufacturer
Membrane tortuosity, τ [–]	6.1	6.1	Eq. (31)
Max. pore radius, δ_{max} [μm]	0.44	0.44	Manufacturer
Mean pore radius, $\bar{\delta}$ [μm]	0.08	0.08	Eq. (32)
Pore standard deviation, σ [–]	0.26	0.26	Eq. (32)
Packing density, $\emptyset$ [–]	0.26	[a]	Manufacturer
Module inner radius, R_m [m]	0.015	[a]	Manufacturer
Membrane module area, A_m [m^2]	0.128	[a]	Manufacturer

[a] Values not reported for confidentiality reasons.

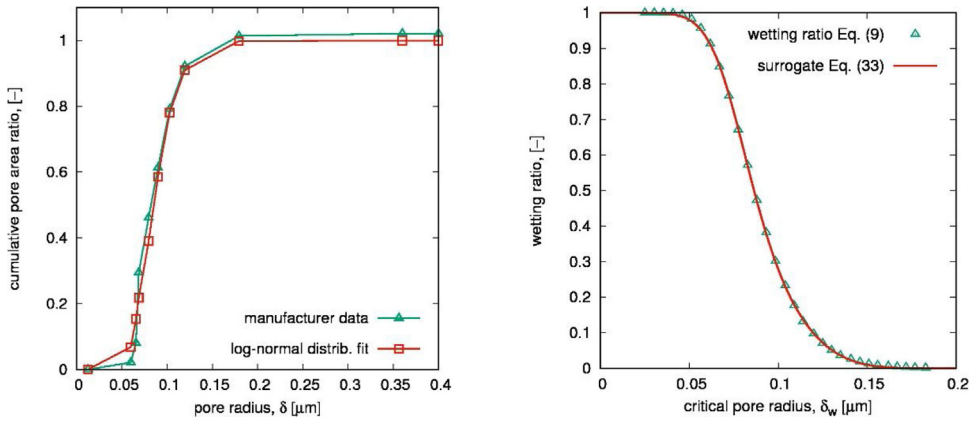


Fig. 5 – Left: comparison of cumulative pore area ratio distribution based on the log-normal pore size distribution in Eq. (32) using the parameters in Table 2, against the manufacturer data. Right: comparison of the wetting ratio expression in Eq. (9) with the surrogate expression in Eq. (33) in terms of the critical pore radius δ_w.

of the radial dimension in the partial differential equations in order for the membrane dry and wet spatial subdomains to be rectangular. A uniform mesh grid consisting of 70 elements was chosen to perform the simulations herein, which provides solutions within <1% of finer discretizations, while retaining computational tractability. With this discretization, a steady-state simulation takes a few minutes to complete on a desktop computer running Windows 7 with Intel® CoreTM i7-4790 CPU at 3.60 GHz and 32GB of RAM.

4. Experimental model verification

4.1. *Lab-scale MBC module*

A comparison between measured and predicted CO_2 removals in the lab-scale MBC is presented in Fig. 6, in terms of the CO_2 absorption flux, Φ [mol m^{-2} s^{-1}] computed as

$$\Phi = \frac{\pi R_m^2 \emptyset}{A_m}[\overline{v_g}(L)\overline{C_{CO_2}}(L) - \overline{v_g}(0)\overline{C_{CO_2}}(0)]. \quad (34)$$

The experimental data are for several flow rates of the two gas mixtures N_2/CO_2 and CH_4/CO_2 (see Table 1), and also correspond to different flow rates of the amine solvent. Overall, the predictions are found to be in excellent agreement with the measurements, showing errors lower than 5%. Notice that such an agreement is quite remarkable given that none of the model parameters are adjusted here, thereby providing a first validation of the main modeling assumptions.

The MBC model correctly predicts the increase in CO_2 absorption flux with a larger inlet gas flowrate, driven by a larger amount of CO_2 in the gas feed. As far as membrane wetting is concerned, non-wetted operation is predicted for all three N_2/CO_2 experiments in Fig. 6A–C, whereas a wetting ratio in the range 5–11% is predicted for the CH_4/CO_2 experiment. This difference between both gas mixtures can be attributed to a higher contact angle in the experiment with N_2/CO_2 ($\theta = 95.3°$) compared with CH_4/CO_2 ($\theta = 92.5°$).

4.2. *Pilot-scale MBC module*

A comparison between measured and predicted CO_2 removals in the pilot-scale MBC module is presented in Fig. 7, also in terms of the CO_2 absorption flux Φ defined in Eq. (34). The experimental data correspond to different flow rates of the amine solvent and of the NG mixture (see Table 1). The MBC model predictions are in good agreement with the measurements, albeit showing larger and more systematic errors, up to 10% overestimation, as compared with the lab-scale results in Fig. 6. A possible explanation for such systematic offsets between the predictions and measurements, could be due to the model currently neglecting the heat generated from the reaction between CO_2 and the amines, which causes the liquid temperature to rise. This scenario is analyzed in more details further on. Another contribution to this offset could be underestimating the mass-transfer resistance near the membrane-liquid interface, especially at lower liquid flow rates, e.g. due to the formation of a boundary film.

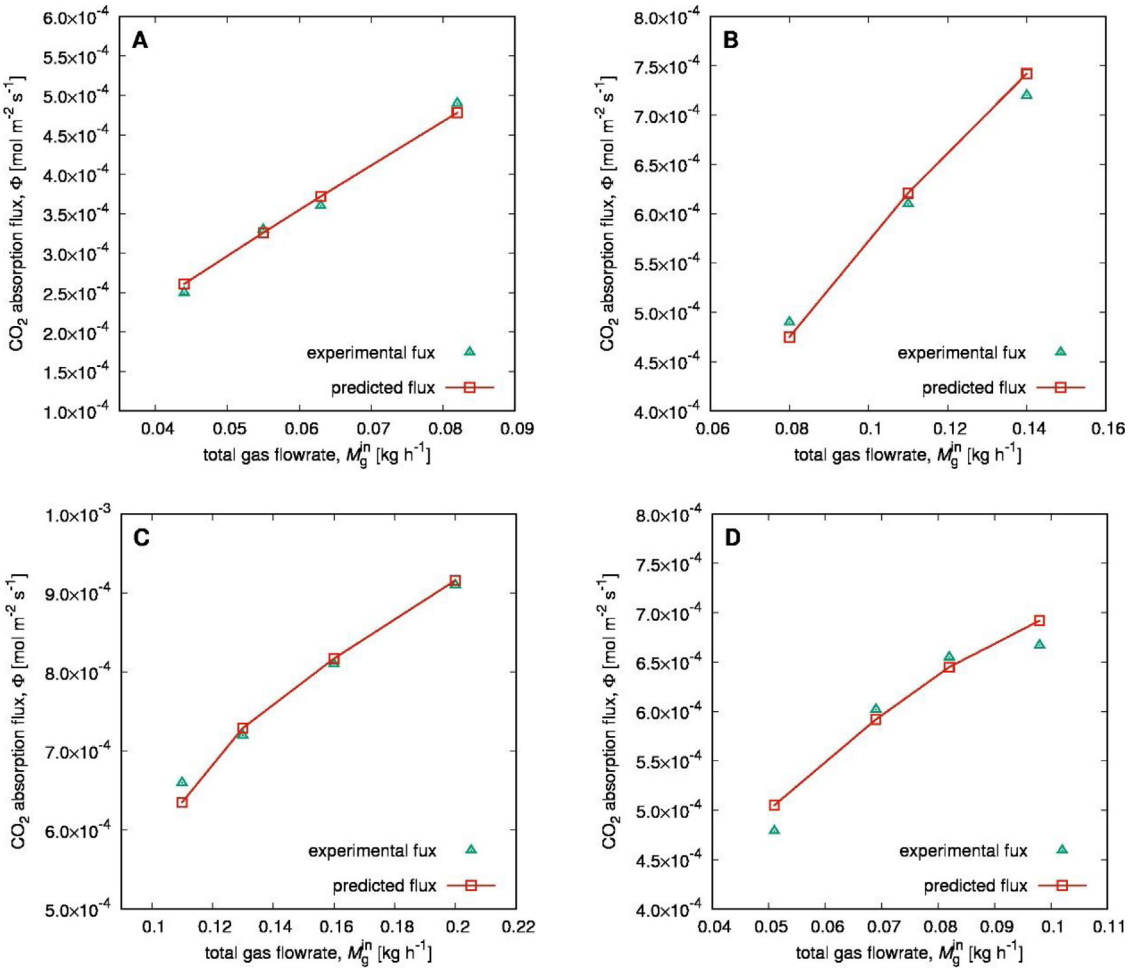


Fig. 6 – Predicted CO_2 absorption fluxes against experimental measurements in lab-scale MBC module. A–C: effect of N_2/CO_2 gas flowrate for fixed solvent flowrates of 0.6 L h^{-1}, 1.2 L h^{-1}, and 1.8 L h^{-1}, respectively; D: effect of CH_4/CO_2 gas flowrate for a fixed solvent flowrate of 1.2 L h^{-1}.

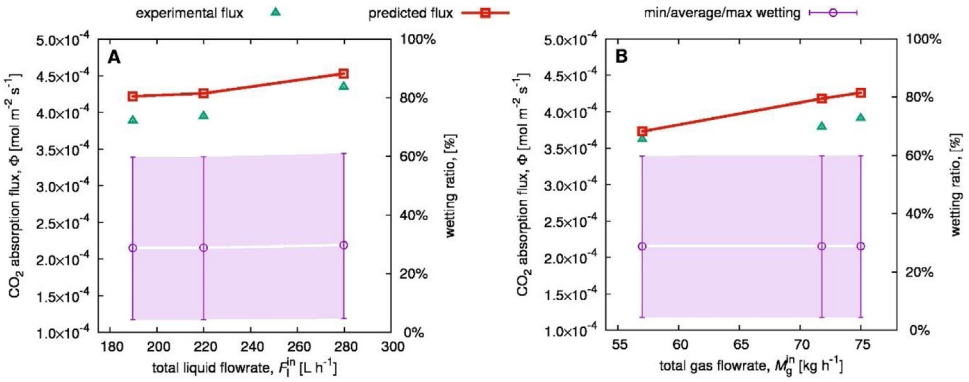


Fig. 7 – Predicted CO_2 absorption fluxes against experimental measurements in pilot-scale MBC module, together with predicted membrane wetting. A: effect of solvent flowrate for a fixed NG flowrate of 75 kg h^{-1}. B: effect of NG flowrate for a fixed solvent flowrate of 220 L h^{-1}.

The model correctly captures the improvement in CO_2 absorption flux on increasing the solvent flowrate in Fig. 7A, and it also predicts a corresponding small increase in the membrane wetting. This extra wetting is due to a higher pressure drop in the shell, and therefore a higher transmembrane pressure, as described in Eqs. (4) and (5). On balance however, the effect of a larger wetting remain small in comparison with the effect of a leaner amine (and hence a larger concentration gradient) in terms of the overall CO_2 mass transfer. These results are also a confirmation that the MBC performance is, to a large extent, dominated by the physicochemical processes taking place in the liquid phase, a behavior that has been reported in the literature previously [Boributh et al., 2011; Goyal et al., 2015].

The model also correctly captures the increase in CO_2 absorption flux for increasing inlet gas flowrates in Fig. 7B, as driven by a larger amount of CO_2 in the gas feed. Also note that, since the pressure drops in the tubes is negligible, see Eq. (4), increasing the inlet gas flowrate has essentially no effect on the wetting ratio.

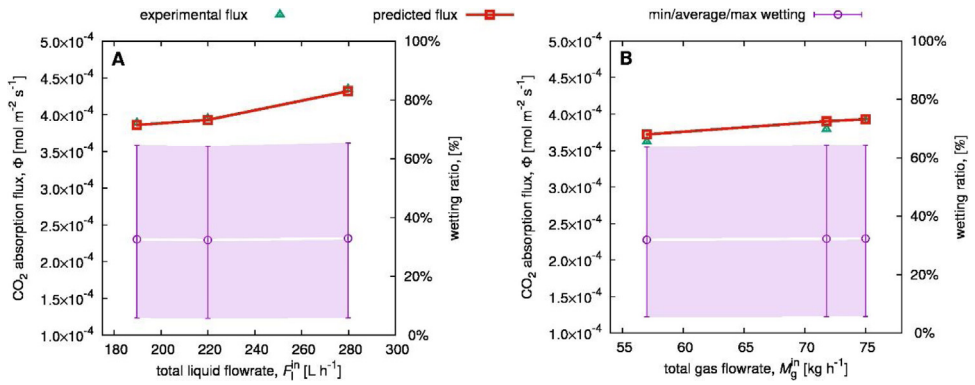


Fig. 8 – Temperature-corrected predictions of CO_2 absorption fluxes against experimental measurements in pilot-scale MBC module, together with predicted membrane wetting. A: variation of the solvent flowrate for a fixed NG flowrate of 75 kg h^{-1}; B: variation of the NG flowrate for a fixed solvent flowrate of 220 L h^{-1}.

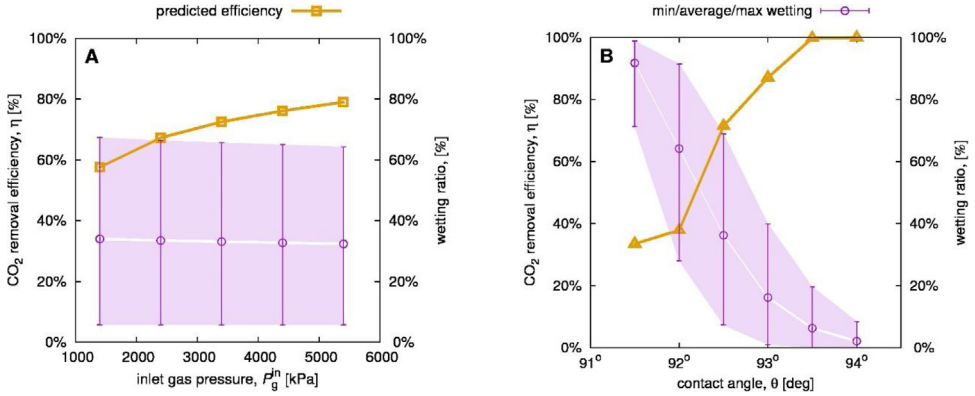


Fig. 9 – Model-based analysis of (vertical) pilot-scale MBC module. The NG gas and solvent flowrates are 75 kg h^{-1} and 220 L h^{-1}, respectively. The solvent temperature is corrected using Eq. (35). A: effect of operating pressure. B: effect of the contact angle.

4.3. *Temperature correction*

This subsection quantifies the effect of a rise in the solvent temperature due to the exothermic reaction between CO_2 and the amines. An increase in the solvent temperature leads to a reduction in surface tension, therefore causing extra wetting of the membrane according to Eq. (3) and a reduction in the CO_2 flux through the membrane. The temperature difference, ΔT_l [K] between the lean amine fed to the MBC module and the enriched amine outlet can be estimated by means of a lumped energy balance under adiabatic conditions [Li et al., 2017],

$$\rho_l F_l^{in} C_p \, \Delta T_l = \Phi A_m \, \Delta H_r. \tag{35}$$

where the term ΦA_m [mol s^{-1}] describes the overall rate of CO_2 removal; and the specific heat capacity of the amine solvent and the enthalpy of reaction are set to $C_p = 3600\,J\,kg^{-1}K^{-1}$ [Weiland et al., 1997] and $\Delta H_r = 60\,000\,J\,mol^{-1}$ [Kabadi, 2007], respectively, in a first approximation.

Based on Eq. (35) and the data in Table 1, the solvent temperature in the pilot-scale MBC module is predicted to increase by 10–14 K. This rise, in turn, corresponds to a reduction in the solvent surface tension from 0.046 to about 0.044 N m^{-1}. The results of the MBC model simulations with the corrected surface tension values are presented in Fig. 8. The predicted CO_2 absorption fluxes are now in close agreement with the measured efficiencies, after an increase in the predicted membrane wetting. By contrast, the solvent temperature in the lab-scale MBC module is predicted to increase by a few degrees only, which does not have as large an impact on the computed fluxes in Fig. 6. The larger temperature rise in the pilot-scale module is due to the liquid-to-CO_2-gas-absorbed (L/G) ratio therein being only one-third of the L/G ratio in the lab-scale module. A low L/G ratio as in the pilot-scale module is comparable to conventional packed columns, and is typically preferred in practice since it reduces the energy needed for solvent regeneration. In sum, this cursory analysis confirms that one should not neglect the temperature rise in the solvent to empower more accurate performance predictions in pilot-scale (or larger-scale) MBC modules. Clearly, this calls for the development of a detailed energy balance alongside the mass balance equations in the MBC model, as part of future work.

5. Model-based analysis

This section of the paper presents a model-based analysis of MBC for natural gas sweetening, with a focus on high-pressure operation and membrane wetting. The analysis is conducted for the pilot-scale MBC module, and applies the temperature correction discussed earlier.

5.1. *Is high-pressure MBC operation advantageous for CO_2 removal?*

The benefits of high-pressure MBC operation in natural sweeting applications, where it can lead to significant savings with regards to compression costs, are well established [Mansourizadeh and Ismail, 2009; Zhang and Wang, 2013]. This subsection investigates whether or not high-pressure

operation also presents advantages in terms of the MBC performance for CO_2 removal. Physically, the diffusivity of CO_2 in NG is known to decrease at higher pressure, thus increasing the overall mass transfer resistance; whereas an increase in the CO_2 partial pressure will enhance the mass transfer, and so will a lower gas velocity by increasing the residence time of the gas. Predicting the net effect of raising the operating pressure on the CO_2 absorption flux and the CO_2 removal efficiency is therefore challenging.

The graph in Fig. 9A shows the effect of varying the operating pressure in the (vertical) pilot-scale MBC on the CO_2 removal efficiency, η [–] given by

$$\eta = 1 - \frac{\overline{v_g}(0)\overline{C_{CO_2}}(0)}{\overline{v_g}(L)\overline{C_{CO_2}}(L)}. \quad (36)$$

The MBC model predicts an improvement in CO_2 removal efficiency from about 60% to 80% in increasing both the gas and liquid pressures from 1400 kPa to 5400 kPa (maintaining a transmembrane pressure of $\Delta P_{TMPD} = 30$ kPa along the fibers in order to prevent gas bubbling). This corresponds to an improvement in CO_2 absorption flux Φ by nearly 40%. On balance, the increase in mass transfer driving force and the longer residence time thus clearly dominate over the lower diffusivity in terms of CO_2 absorption and removal efficiency. These results are consistent with those previously reported by Faiz and Al-Marzouqi (2010), although their model could not predict the effect of varying operating conditions on membrane wetting or the evolution of membrane wetting along a hollow fiber. In particular, the model only predicts small variations in the wetting ratio in operating the MBC at different pressures, and therefore the performance improvement at high pressure is not associated with a reduction in membrane wetting.

From a process engineering standpoint, higher efficiency in terms of CO_2 removal in high-pressure MBC compared with atmospheric operation could enable a reduction of the absorber volume (i.e. lower membrane area and module size) and/or a lower solvent flowrate (i.e. lower solvent regeneration and pumping energy) in order to meet a certain CO_2 purity specification.

5.2. *How large is the effect of module orientation in high-pressure MBC?*

The concentration profiles of CO_2 and amines around a single fiber are shown in Fig. 10A, for the pilot-scale module in vertical orientation, operated under 5400 kPa and with other conditions as given in Table 1. The three graphs show that the wetting ratio ζ (or, equivalently, the wetting radius r_w) varies significantly along the fiber axis, from about 6% at the gas inlet to over 64% at the gas outlet. This variation is mainly due to the static head in the liquid phase, while the pressure drops remain small in comparison.

On the left graph in Fig. 10A, the CO_2 concentration in the tube is the highest at the gas inlet, $z = 2$ m, and decreases along the fiber. In this vertical configuration, the CO_2 removal efficiency is rather low, around $\eta \approx 79\%$, due to significant wetting of the membrane. Recall also that the gas phase is uniform in each tube cross-section per the modeling assumptions in Section 2.2. In the dry part of the membrane, the CO_2 concentration is decreasing slightly in the radial direction due to diffusive transfer limitation, and then shows a discontinuity at gas–liquid interface, with a near-zero CO_2 concentration across the liquid phase.

The center and right graphs in Fig. 10A show that the MDEA and PZ amine concentrations in the shell are the highest at the liquid inlet, $z = 0$ m, and decrease along the fiber axis due to the reactions with CO_2. It is noticeable that the PZ concentration decreases faster than the MDEA concentration, due to PZ having a higher reactivity with CO_2 than MDEA. These plots also depict steep gradients in MDEA and PZ concentrations across the wetted-part of the membrane, as well as some variations across the liquid phase, which justify the use of 2-d modeling to describe radial diffusive mass transfer in the membrane and shell sections.

For comparison, the concentration profiles shown in Fig. 10B are for the same pilot-scale module, now in horizontal orientation. The wetting ratio is predicted to be much smaller and about constant along the fiber length, around 6%, due to the transmembrane pressure difference no longer being subject to the liquid static head; see Eq. (4). Consequently, the CO_2 removal efficiency in horizontal orientation improves enormously, reaching 99.99% (residual concentration of $\overline{C_{CO_2}}(0) \approx 1.5 \times 10^{-2}$ mol m^{-3}), as compared with a mere 79% removal in vertical orientation. Also notice that a majority of the PZ amine is depleted at the horizontal module outlet. By contrast, the performance of the lab-scale module, whose length is much shorter than the pilot-scale one (see Table 2), does not improve significantly in changing the orientation to horizontal (results not shown).

Overall, this analysis suggests that, for the PTFE hollow-fiber membrane at hand, the vertical mode of operation might not be viable in pilot-scale and larger-scale applications where the fibers are several meters long. For such tall modules, the effect of liquid static head could result in the bottom section of the membrane being fully wetted, thereby reducing the CO_2 absorption flux dramatically, or even making it infeasible to reach CO_2 purities down to the ppm level. The vertical mode of operation is nonetheless advantageous in practice since it has a much lower physical footprint than horizontal operation, especially on an offshore platform [Quek et al., 2015]. As part of future work, it will be interesting, to use the MBC model for targeting improvements in the membrane material, amine solvent and operating conditions all together, in order for the vertical mode of operation to become viable in full-scale industrial applications. For instance, the graph in Fig. 9B reports predictions of the CO_2 removal efficiency for (hypothetical) membranes having contact angles with the amine solvent in the range between 91.5° and 94.0°. The efficiency increases steeply over this range, as a driven by a large reduction in membrane wetting. Moreover, the MBC model predicts that CO_2 removal efficiencies as large as those obtained in horizontal orientation could be obtained in the vertical pilot-scale module by using a PTFE membranes with higher hydrophobicity/contact angle.

6. Conclusions and future research directions

This paper has developed a mathematical model of high-pressure MBC using chemical solvents, which describes the effect of membrane pore-size distribution and operating conditions on membrane wetting and CO_2 absorption. A verification of the model has been conducted for both lab-scale and pilot-scale MBC modules, showing a close agreement of the predictions with measured CO_2 absorption flux at various

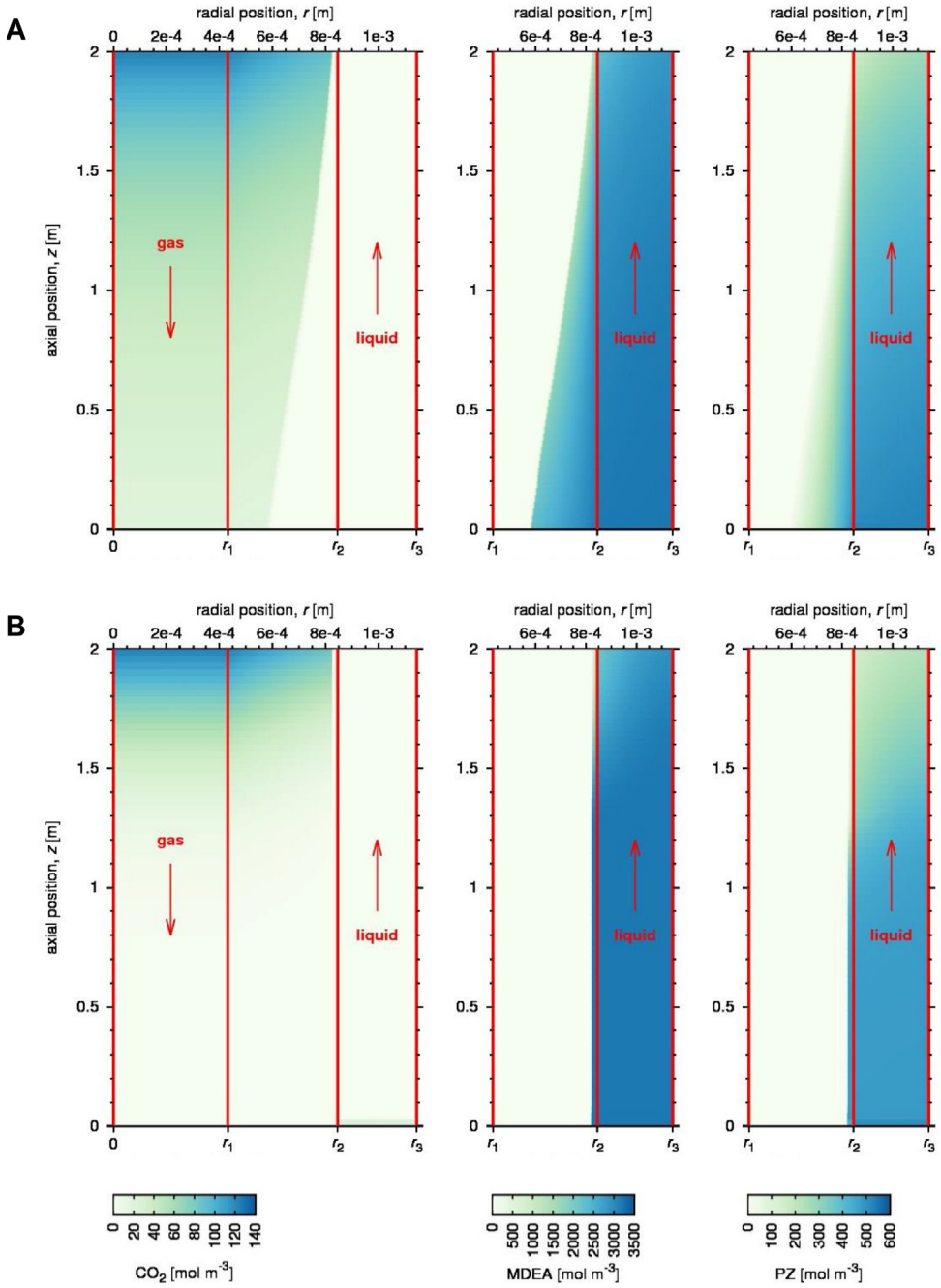


Fig. 10 – Concentration profiles of CO_2 (left), MDEA (center) and PZ (right) for a single fiber of the pilot-scale MBC module. The NG and solvent flowrates are 75 kg h^{-1} and 220 L h^{-1}, respectively. The solvent temperature is corrected using Eq. (35). A: vertical module orientation. B: horizontal module orientation.

gas and liquid flowrate, subject to a temperature correction to account for the heat of reaction in the liquid phase. Next, a model-based analysis of MBC for natural gas sweetening has been presented, with a focus on high-pressure operation and the effect of membrane wetting. The results confirm the advantages of a pressurized operation in terms of CO_2 removal efficiency. Moreover, a comparison between vertical and horizontal modes of operation has shown that the CO_2 removal efficiency in the latter can be vastly superior as it is not subject to the liquid static head. A vertical mode of operation could nonetheless become competitive if membrane materials with improved hydrophobicity were used.

A natural continuation of this work entails the application of systematic, model-based optimization methods to improve the design and operation of full-scale MBC modules. In particular, a comprehensive techno-economic analysis should also include the solvent regeneration unit in the assessment. In addition to optimizing such decisions as the gas and liquid flowrates, operating pressure and temperature, module length and specific area, one could consider optimal solvent selection as well as the optimal arrangement of MBC modules into multistage cascades. Finally, one could also envisage using the MBC model to guide the development of improved membrane materials.

Acknowledgements

The authors gratefully acknowledge PETRONAS for financial support and for providing the experimental data.

Appendix A. Transport and reaction kinetic correlations

- Macroscopic reaction rates between the CO_2 and the amine solvent are assumed to follow mass-action kinetics,

$$R_{CO_2} = -k_{MDEA}\, C_{CO_2}\, C_{MDEA} - k_{PZ}\, C_{CO_2}\, C_{PZ} \quad (A.1)$$

$$R_{MDEA} = -k_{MDEA}\, C_{CO_2}\, C_{MDEA} \quad (A.2)$$

$$R_{PZ} = -k_{PZ}\, C_{CO_2}\, C_{PZ} \quad (A.3)$$

with the reaction rate constants given by [Ko and Li, 2000; Sun et al., 2005; Lu et al., 2007]

$$k_{MDEA} = 4.01 \times 10^5 \exp\left(-\frac{5400}{T}\right) \quad (A.4)$$

$$k_{PZ} = 4.49 \times 10^9 \exp\left(-\frac{5712}{T}\right) \quad (A.5)$$

- Henry's constant for CO_2 in amine solutions at various temperatures is estimated based on N_2O analogy [Versteeg and Van Swaaij, 1988; Wang et al., 2013],

$$H_{CO_2} = H_{N_2O,l}\frac{H_{CO_2,H_2O}}{H_{N_2O,H_2O}} \quad (A.6)$$

where Henry's constants for N_2O and CO_2 in water are taken as [Versteeg and Van Swaaij, 1988]

$$H_{CO_2,H_2O} = 2.82 \times 10^6 \exp\left(-\frac{2044}{T}\right) \quad (A.7)$$

$$H_{N_2O,H_2O} = 8.55 \times 10^6 \exp\left(-\frac{2284}{T}\right) \quad (A.8)$$

Henry's constant for N_2O in amine solution, $H_{N_2O,l}$ is described by a semi-empirical model correlating the excess Henry's coefficient as [Bensetiti et al., 1999]

$$\ln H_{N_2O,l} = \phi_{MDEA} \ln H_{N_2O,MDEA} + \phi_{PZ} \ln H_{N_2O,PZ} + \phi_{H_2O} \ln H_{N_2O,H_2O} + \phi_{MDEA}\phi_{H_2O}\left[-2.899 + \frac{1405.43}{T}\right] \quad (A.9)$$

with ϕ_i the volume fraction of species i; and the solubility of N_2O in pure amine solvent $i \in \{MDEA, PZ\}$ taken as [Wang et al., 1992]

$$H_{N_2O,MDEA} = H_{N_2O,PZ} = 1.52 \times 10^5 \exp\left(-\frac{1312.7}{T}\right) \quad (A.10)$$

- The diffusivity of CO_2 in liquid is also estimated based on the analogy of N_2O diffusivity in solution [Versteeg and Van Swaaij, 1988]

$$D_{CO_2,l} = D_{N_2O,l}\frac{D_{CO_2,H_2O}}{D_{N_2O,H_2O}} \quad (A.11)$$

with the diffusivities of CO_2 and N_2O in water given by

$$D_{CO_2,H_2O} = 2.35 \times 10^{-6} \exp\left(-\frac{2119}{T}\right) \quad (A.12)$$

$$D_{N_2O,H_2O} = 5.07 \times 10^{-6} \exp\left(-\frac{2371}{T}\right) \quad (A.13)$$

The diffusion coefficient of N_2O in liquid amine solution is estimated using the modified Stokes–Einstein relation [Mandal et al., 2003;Wang et al., 2013]

$$D_{N_2O,l} = D_{N_2O,H_2O}\left(\frac{\mu_{H_2O}}{\mu_l}\right)^{0.6} \quad (A.14)$$

where the viscosities μ_{H_2O} and μ_l of the water and amines, respectively, are obtained from the package 'UNIQUAC-RK'. Likewise, the temperature-corrected diffusivities of MDEA and PZ amines in the liquid phase are correlated using the modified Stokes-Einstein relation [Wang et al., 2013]

$$D_{MDEA,l} = D_{MDEA,H_2O}\frac{T}{273}\left(\frac{\mu_{H_2O}}{\mu_l}\right)^{0.6} \quad (A.15)$$

$$D_{PZ,l} = D_{PZ,H_2O}\frac{T}{273}\left(\frac{\mu_{H_2O}}{\mu_l}\right)^{0.6} \quad (A.16)$$

where the diffusivities of MDEA and PZ in water, and the liquid and water dynamic viscosities are obtained from the package 'UNIQUAC-RK'. The diffusivity of CO_2 in NG was estimated from empirical correlations based on kinetic gas theory [Cussler, 2009; Bird et al., 1960]

$$D_{CO_2,NG} = \frac{T^{1.75}\left(1/M_{CO_2} + 1/M_{NG}\right)^{1/2}}{10^5\, P\left[\left(\sum V_{CO_2}\right)^{1/3} + \left(\sum V_{NG}\right)^{1/3}\right]^2} \quad (A.17)$$

where M_{CO_2} and M_{NG} stand for the molecular weights of CO_2 and NG; and the summations of atomic diffusion volumes for the species of the CO_2–NG gas mixture are taken as $\sum V_{CO_2} = 26.9$ and $\sum V_{NG} = 24.42$. Lastly, the diffusivity of CO_2 in N_2 gas was obtained from the package 'Advanced Peng–Robinson'.

The numerical values are reported in Table A1 correspond to the temperature and pressure conditions in the lab- and pilot-scale MBC modules (see Table 1).

Table A1 – Model parameters used in the lab and pilot plant MBC simulations.

Parameters	N_2-CO_2 (lab)	CH_4-CO_2 (lab)	NG(pilot)
Diffusivity of CO_2 in gas, $D_{CO_2,g}$ [m s^{-2}]	1.44×10^{-6}	1.50×10^{-6}	3.23×10^{-7}
Diffusivity of CO_2 in liquid, $D_{CO_2,l}$ [m s^{-2}]	1.00×10^{-9}	1.46×10^{-9}	1.46×10^{-9}
Diffusivity of MDEA in liquid, $D_{MDEA,l}$ [m s^{-2}]	1.39×10^{-10}	2.37×10^{-10}	2.37×10^{-10}
Diffusivity of PZ in liquid, $D_{PZ,l}$ [m s^{-2}]	3.26×10^{-10}	5.32×10^{-10}	5.31×10^{-10}
Reaction rate constant of MDEA, k_{MDEA} [m^3 mol^{-1} s^{-1}]	4.01×10^{-3}	9.83×10^{-3}	9.83×10^{-3}
Reaction rate constant of PZ, k_{PZ} [m^3 mol^{-1} s^{-1}]	15.5	40.0	40.0
Henry's constant, H_{CO_2} [m^3 Pa mol^{-1}]	2878	3636	3588
Density of gas, ρ_g [kg m^{-3}]	13.3	8.5	49.2
Density of liquid, ρ_l [kg m^{-3}]	994	986	986
Dynamic viscosity of liquid, μ_l [kg m^{-1} s^{-1}]	2.49×10^{-3}	1.73×10^{-3}	1.74×10^{-3}
Surface tension of amine solvent, γ [N m^{-1}]	0.046	0.046	0.046

References

Al-Marzouqi, M.H., El-Naas, M.H., Marzouk, S.A.M., Al-Zarooni, M.A., Abdullatif, N., Faiz, R., 2008. Modeling of CO_2 absorption in membrane contactors. Sep. Purif. Technol. 59 (3), 286–293.

Bensetiti, Z., Iliuta, I., Larachi, F., Grandjean, B.P.A., 1999. Solubility of nitrous oxide in amine solution. Ind. Eng. Chem. Res. 38, 328–332.

Bird, R.B., Lightfoot, E.N., Stewart, W.E., 1960. Transport Phenomena. John Wiley & Sons.

Boributh, S., Assabumrungrat, S., Laosiripojana, N., Jiraratananon, R., 2011. A modeling study on the effects of membrane characteristics and operating parameters on physical absorption of CO_2 by hollow fiber membrane contactor. J. Membr. Sci. 380 (1–2), 21–33.

Boucif, N., Corriou, J.P., Roizard, D., Favre, E., 2012. Carbon dioxide absorption by monoethanolamine in hollow fiber membrane contactors: a parametric investigation. AIChE J. 58 (9), 2843–2855.

Chabanon, E., Roizard, D., Favre, E., 2013. Modeling strategies of membrane contactors for post-combustion carbon capture: a critical comparative study. Chem. Eng. Sci. 87, 393–407.

Cui, L., Ding, Z., Liu, L., Li, Y., 2015. Modelling and experimental study of membrane wetting in microporous hollow fiber membrane contactors. Can. J. Chem. Eng. 93 (7), 1254–1265.

Cussler, E.L., 2009. Diffusion: Mass Transfer in Fluid Systems, 3rd edition. Cambridge University Press, New York.

Favre, E., 2011. Membrane processes and post-combustion CO_2 capture: challenges and prospects. Chem. Eng. J. 171, 782–793.

Faiz, R., Al-Marzouqi, M., 2010. CO_2 removal from natural gas at high pressure using membrane contactors: model validation and membrane parametric studies. J. Membr. Sci. 365, 232–241.

Gabelman, A., Hwang, S.T., 1999. Hollow fiber membrane contactors. J. Membr. Sci. 159, 61–106.

Goyal, N., Sumanm, S., Gupta, S.K., 2015. Mathematical modeling of CO_2 separation from gaseous-mixture using a hollow-fiber membrane module: physical mechanism and influence of partial-wetting. J. Membr. Sci. 474, 64–82.

Happel, J., 1959. Viscous flow relative to arrays of cylinders. AIChE J. 5, 174–177.

He, X., Hägg, M.B., 2012. Membranes for environmentally friendly energy processes. Membranes 2, 706–726.

Hoff, K.A., (Ph.D. thesis) 2003. Modeling and experimental study of carbon dioxide absorption in a membrane contactor. Norwegian University of Science and Technology.

Hoff, K.A., Julliussen, O., Falk-Pedersen, O., Svendsen, H.F., 2004. Modeling and experimental study of carbon dioxide absorption in alkalanolamine solutions using a membrane contactor. Ind. Eng. Chem. Res. 43, 4908–4921.

Hoff, K.A., Svendsen, H.F., 2013. CO2 absorption with membrane contactors vs. packed absorbers – challenges and opportunities in post combustion capture and natural gas sweetening. Energy Procedia 37 (1876), 952–960.

Hoff, K.A., Svendsen, H.F., 2014. Membrane contactors for CO_2 absorption – application, modelling, and mass transfer effects. Chem. Eng. Sci. 116, 331–341.

IEA, 2017. 2016 International Energy Outlook, Report Number DOE/EIA-0484(2016), Available online from: https://www.eia.gov/outlooks/ieo/ (accessed 06.09.17).

Iversen, S.B., Bhatia, V.K., Dam-Johansen, K., Jonsson, G., 1997. Characterization of microporous membranes for use in membrane contactors. J. Membr. Sci. 130, 205–217.

Kabadi, V.N., 2007. Heat of Dissolution Measurements for CO_2 in Mixed Alkanolamine Solvents, Final Report DE-FG26-03NT41912. North Carolina A&T State University, Greensbor.

Kang, G., Chan, Z.P., Saleh, S.B.M., Cao, Y., 2017. Removal of high concentration CO_2 from natural gas using high pressure membrane contactors. Int. J. Greenh. Gas Control 60, 1–9.

Ko, J.J., Li, M.H., 2000. Kinetics of absorption of carbon dioxide into solutions of N-methyldiethanolamine + water. Chem. Eng. Sci. 55, 4139–4147.

Li, S., Pyrzynski, T.J., Klinghoffer, N.B., Tamale, T., Zhong, Y., Aderhold, J.L., Zhou, S.J., Meyer, H.S., Ding, Y., Bikson, B., 2017. Scale-up of PEEK hollow fiber membrane contactor for post-combustion CO_2 capture. J. Membr. Sci. 527, 92–101.

Lu, J.G., Zheng, Y.F., Cheng, M.D., 2008. Wetting mechanism in mass transfer process of hydrophobic membrane gas absorption. J. Membr. Sci. 308 (1–2), 180–190.

Lu, J.G., Zheng, Y.F., Cheng, M.D., Wang, L.J., 2007. Effects of activators on mass-transfer enhancement in a hollow fiber contactor using activated alkanolamine solutions. J. Membr. Sci. 289 (1–2), 138–149.

Mandal, B.P., Biswas, A.K., Bandyopadhyay, S.S., 2003. Absorption of carbon dioxide into aqueous blends of 2-amino-2-methyl-1-propanol and diethanolamine. Chem. Eng. Sci. 58 (18), 4137–4144.

Mansourizadeh, A., Ismail, A.F., 2009. Hollow fiber gas–liquid membrane contactors for acid gas capture: a review. J. Hazard. Mater. 171, 38–53.

Mosadegh-Sedghi, S., Rodrigue, D., Brisson, J., Iliuta, M.C., 2012. Wetting phenomenon in membrane contactors – causes and prevention. J. Membr. Sci. 452, 332–353.

Oh, M., Pantelides, C.C., 1996. A modelling and simulation language for combined lumped and distributed parameter systems. Comput. Chem. Eng. 20, 611–633.

Paul, S., Ghoshal, A.K., Mandal, B., 2007. Removal of CO_2 by single and blended aqueous alkanolamine solvents in hollow-fiber membrane contactor: modeling and simulation. Ind. Eng. Chem. Res. 46, 2576–2588.

Quek, V.C., Azmil, A.A., Chan, Z.P., Cao, Y., Kang, G., Li, M., Jia, J., 2015. Process and system for treating natural gas feedstock. WO Patent Application PCT/CN2013/000,840.

Rangwala, H.A., 1996. Absorption of carbon dioxide into aqueous solutions using hollow fiber membrane contactors. J. Membr. Sci. 112 (2), 229–240.

Rezakazemi, M., Niazi, Z., Mirfendereski, M., Shirazian, S., Mohammadi, T., Pak, A., 2011. CFD simulation of natural gas sweetening in a gas–liquid hollow-fiber membrane contactor. Chem. Eng. J. 168 (3), 1217–1226.

Rongwong, W., Fan, C., Liang, Z., Rui, Z., Idem, R.O., Tontiwachwuthikul, P., 2015. Investigation of the effects of operating parameters on the local mass transfer coefficient and membrane wetting in a membrane gas absorption process. J. Membr. Sci. 490, 236–246.

Sun, W.C., Yong, C.B., Li, M.H., 2005. Kinetics of the absorption of carbon dioxide into mixed aqueous solutions of 2-amino-2-methyl-l-propanol and piperazine. Chem. Eng. Sci. 60 (2), 503–516.

TransCanada, 2016. Gas Quality Specifications-TransCanada and other pipelines. Available at: http://www.tccustomerexpress.com/docs/Gas_Quality_Specifications_Fact_Sheet.pdf (accessed 06.09.17).

Versteeg, G.F., Van Swaaij, W.P.M., 1988. Solubility and diffusivity of acid gases (carbon dioxide, nitrous oxide) in aqueous alkanolamine solutions. J. Chem. Eng. Data 33 (1), 29–34.

Wang, R., Zhang, H.Y., Feron, P.H.M., Liang, D.T., 2005. Influence of membrane wetting on CO_2 capture in microporous hollow fiber membrane contactors. Sep. Purif. Technol. 46 (1–2), 33–40.

Wang, Y.W., Xu, S., Otto, F.D., Mather, A.E., 1992. Solubility of N_2O in alkanolamines and in mixed solvents. Chem. Eng. J. 92, 31–40.

Wang, Z., Fang, M., Yu, H., Wei, C.-C., Luo, Z., 2013. Experimental and modeling study of trace CO_2 removal in a hollow-fiber membrane contactor, using CO_2-loaded monoethanolamine. Ind. Eng. Chem. Res. 52, 18059–18070.

Weiland, R.H., Dingman, J.C., Cronin, D.B., 1997. Heat capacity of aqeous monoethanolamine, diethanolamine, N-methyldiethanolamine, and

N-methyldiethanolamine-based blends with carbon dioxide. J. Chem. Eng. Data 42, 1004–1006.
Zhang, Y., Wang, R., 2013. Gas–liquid membrane contactors for acid-gas removal: recent advances and future challenges. Curr. Opin. Chem. Eng. 2 (2), 255–262.
Zhou, S., Meyer, H., 2014. Sweetening of natural gas by membrane contactor. WO Patent Application PCT/US2014/022,290.
Zydney, A.L., Aimar, P., Meireles, M., Pimbley, J.M., Belfort, G., 1994. Use of the log-normal probability density function to analyze membrane pore size distributions: functional forms and discrepancies. J. Membr. Sci. 91 (3), 293–298.